J Mater Sci: Mater Electron (2017) 28:4914–4924
DOI 10.1007/s10854-016-6140-7

The role of Tb-doping on the structural and functional properties of $Bi_{4-x}Tb_xTi_3O_{12}$ ferroelectric phases with the Aurivillius type structure

Tapati Sarkar[1] · Sergey A. Ivanov[1,2] · Elena A. Fortalnova[3] · Ekaterina D. Politova[2] · Marina G. Safronenko[3] · Per Nordblad[1] · Roland Mathieu[1]

Received: 2 September 2016 / Accepted: 24 November 2016 / Published online: 3 December 2016
© The Author(s) 2016. This article is published with open access at Springerlink.com

Abstract Synthesis, crystal structure, dielectric, and magnetic properties of the Aurivillius phase $Bi_{4-x}Tb_xTi_3O_{12}$ ($x = 0.0, 0.4, 0.6, 0.8$) are reported. The samples were synthesized using standard solid state reaction technique. The thermal stability of the obtained solid solutions was investigated. For $x \leq 0.8$, the samples crystallized in an orthorhombic symmetry. All the samples showed finite second harmonic generation response indicating a non-centrosymmetric structure. The structural data could be refined using the polar orthorhombic space group *B*2*cb*. The orthorhombicity decreases with an increase in the Tb^{3+} concentration. The orthorhombic distortions in these compositions are related to the Bi^{3+}-based perovskite sublattice. Our results indicate that the non-lone pair Tb^{3+} cations preferentially occupy the perovskite sublattice initially, but with an increase in the doping concentration they can partially substitute the Bi^{3+} ions in the fluorite block. Temperature dependent dielectric measurements revealed a decrease in the ferroelectric Curie temperature T_C with an increase in x from $T_C = 904$ K (for $x = 0$) to 877 K (for $x = 0.4$). Further increase in x led to a cross-over to a relaxor-type behavior. Magnetic measurements showed that the samples are paramagnetic down to 5 K.

✉ Tapati Sarkar
tapati.sarkar@angstrom.uu.se

[1] Department of Engineering Sciences, Uppsala University, Box 534, 75121 Uppsala, Sweden

[2] Karpov Institute of Physical Chemistry, ul. Vorontsovo Pole 10, Moscow, Russia 105064

[3] RUDN University, ul. Miklukho-Maklaya 6, Moscow, Russia 117198

1 Introduction

Multiferroic materials exhibiting dipole and spin orderings simultaneously have attracted a lot of attention during the past decade. The renewed interest comes from the possibility of cross-controlling the magnetization and polarization by applying electric and magnetic fields respectively in these materials [1, 2], which provides a route to advanced memory devices [3–5]. Intrinsic multiferroics, where the different ferroic properties occur in one material, are limited in number. Therefore, to obtain new materials with multiferroic properties, one of the most popular approaches is to design new composite multiferroics by doping magnetic (ferroelectric) compounds in ferroelectric (ferromagnetic) matrices [6, 7].

Oxides belonging to the Aurivillius family constitute an important class of materials that have been studied since a long time for their ferroelectric [8, 9] and piezoelectric [10, 11] properties. The general formula of this class of oxides is $(Bi_2O_2)(A_{m-1}B_mO_{3m+1})$, and they consist of an intergrowth between $(Bi_2O_2)^{2+}$ sheets and $(A_{m-1}B_mO_{3m+1})^{2-}$ perovskite-like layers, with *m* being the number of octahedra stacked along the direction perpendicular to the sheets, and A, and B, are the 12-fold, and sixfold coordination sites of the perovskite slab, respectively. $Bi_4Ti_3O_{12}$ (BTO) (where $m = 3$) has been widely studied for its ferroelectric properties since the early works of Smolenskii et al. [12] and Subbarao [13]. However, the potential of Ln-doped BTO materials for commercial applications as promising alternatives for ferroelectric random access memories (FeRAMs) was realized much later [14]. The magnetic properties can be enhanced via structural modification using appropriate doping. Recently, a lot of work has focused on layered perovskites in general [15], and bismuth layer-structured ferroelectrics in particular [16]. Several

investigations have also focused on doping magnetic ions in $Bi_4Ti_3O_{12}$ [17–23]. However, the reported magnetic properties in these materials are quite weak even at low temperatures.

The BTO structure is relatively complex (Fig. 1), containing six crystallographically distinct oxygen sites and four different cation sites, viz. two distinct Ti sites (the 'B' sites of the perovskite block) and two distinct Bi sites (the perovskite 'A' site and the interlayer $[Bi_2O_2]$ site). In the present article, we report on the synthesis and detailed structural, dielectric, and magnetic studies of single phase Tb-doped BTO.

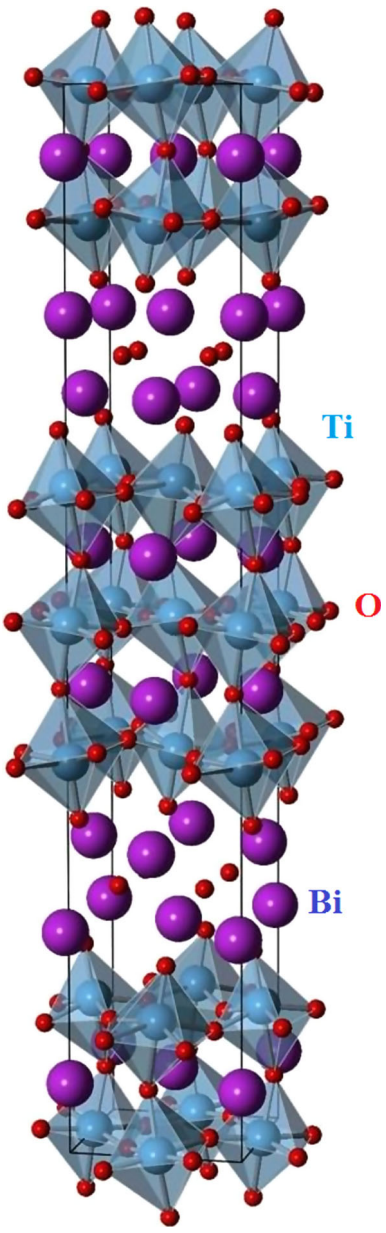

Fig. 1 Schematic representation of the BTO structure. Bi—*purple spheres*, TiO_6 octahedra—*blue*, O—*red spheres*. Figure prepared using VESTA [24] (Color figure online)

2 Experimental details

$Bi_{4-x}Tb_xTi_3O_{12}$ (BTTO) solid solutions with x = 0.0, 0.4, 0.6, and 0.8 were prepared by traditional solid state reaction technique. Stoichiometric quantities of Bi_2O_3, Tb_4O_7, and TiO_2 were thoroughly ground, pelletized, and dried at 800 °C within 2 h for removal of possible adsorbed moisture and carbon dioxide. Preparation of BTTO solid solutions was carried out by solid-state reaction via the equation:

$$[(4-x)/2]Bi_2O_3 + 3TiO_2 + (x/4)Tb_4O_7 \rightarrow Bi_{4-x}Tb_xTi_3O_{12} + (x/4)O_2$$

The samples were annealed at 700, 800, and 900 °C for 10 h at each temperature to obtain the desired chemical phase. A heating rate of 10 °C/min was used. Calcination occurred at 800 °C and the samples were sintered at 900 °C for further densification. More details about the synthesis can be found in reference [25].

The phase interactions at each stage of the synthesis process were monitored using simultaneous thermogravimetry and differential thermal analysis (DTA/TG) using SDT Q600 thermoanalyzer (Pt–Pt/Rh thermocouple) in the temperature range 25–1250 °C in air. The heating rate was varied between 5 and 10 °C/min. It was found that phase formation of the BTTO powders occurred at ~500 °C.

The cation composition was determined by energy dispersive spectroscopy (EDS) analysis using an Epsilon1 microanalyzer (PanAnalytical).

The phase purity of the prepared ceramic samples was monitored by X-ray powder diffraction (XRPD) patterns obtained with a D-5000 diffractometer using Cu-K_α radiation. The samples were crushed into powder in an agate mortar and suspended in ethanol. A Si substrate was covered with several drops of the resulting suspension, leaving randomly oriented crystallites after drying. The XRPD data for Rietveld analysis were collected at room temperature on a Bruker D8 Advance diffractometer (Ge monochromatized Cu $K_{\alpha1}$ radiation, Bragg–Brentano geometry, DIFFRACT plus software) in the 2θ range 10°–152° with a step size of 0.02° (counting time was 15 s per step). The slit system was selected to ensure that the X-ray beam was completely within the sample for all 2θ angles. Structural refinements were performed by the Rietveld method using the FULLPROF program suite [26].

The evolution of the crystal structure with increase in x was also studied using infrared (IR) spectroscopy on a IR-Fourier spectrometer FSM-1202 in a continuous

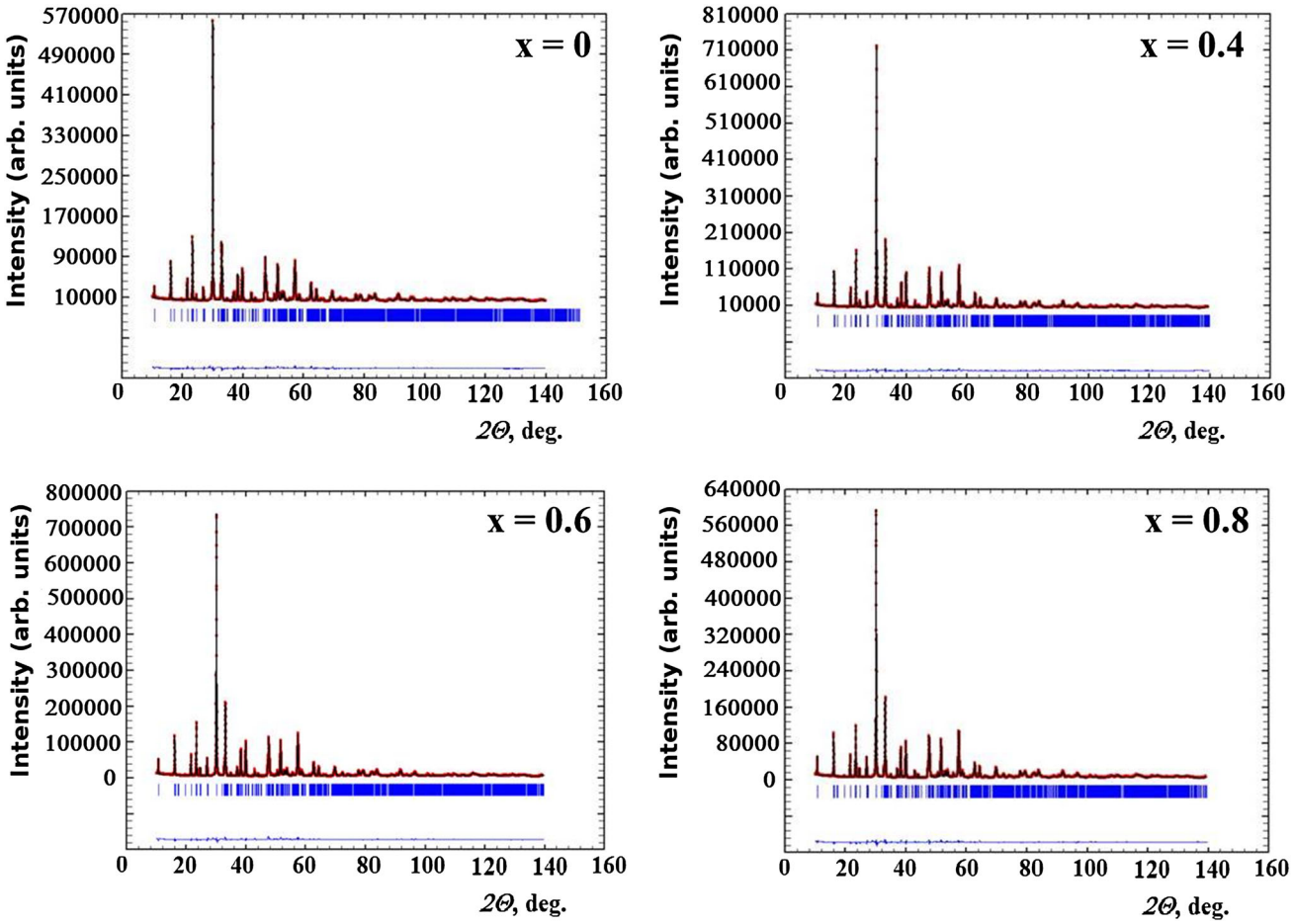

Fig. 2 X-ray diffraction patterns of BTTO at room temperature along with the fit and residue. *Blue tick marks* indicate the Bragg reflections (Color figure online)

registration mode in the frequency range 1500–400 cm^{-1}. For the IR studies, the samples were mixed with dry KBr in the ratio 1:100 to form pellets.

The second harmonic generation (SHG) analysis of the BTTO ceramics was performed at room temperature using a Nd-laser ($\lambda_\omega = 1.064$ μm). SiO_2 was used as an etalon. The presence of second harmonic laser irradiation signal at $\lambda_{2\omega} = 0.532$ μm indicates the existence of a non-centrosymmetric phase in the tested sample [27]. When the dimension of the ceramic crystallites is very small (~2–3 μm), the intensity of the second harmonic laser irradiation ($I_{2\omega}$) is directly proportional to the effective quadratic optical polarization, which increases with increase in non-centrosymmetry of the medium.

Dielectric spectroscopy measurements were performed in the frequency range 10^2–10^6 Hz and the temperature range 298–1023 K, using an Agilent 4284A Precision LCR Meter. Silver electrodes were pasted on opposite planes of a pellet to form a parallel plate capacitor and heated at 800 °C. The heating rate used in the experiments was 5 K/min. The dc magnetic susceptibilty measurements were performed using a Quantum Design superconducting quantum interference device magnetometer in the temperature range 5–320 K.

3 Results and discussion

3.1 X-ray powder diffraction (XRPD)

The XRPD patterns of the BTTO samples are shown in Fig. 2. Pure BTO can be indexed by the JCPDS card (No. 35–0795). As can be seen from Fig. 2, there is very little qualitative difference between the patterns of BTTO and pure BTO. We see a systematic shift of the reflections to lower 2θ values that arises due to the difference between the ionic radii [28] of Tb^{3+} (1.04 Å) and Bi^{3+} (1.17 Å). No secondary phases were found within the detection limit of our XRPD set up.

All the XRPD patterns could be indexed in an orthorhombic symmetry. Careful inspection of the patterns revealed no deviation from orthorhombic symmetry within

Table 1 Results of the Rietveld refinements of the crystal structure at room temperature using XRPD data, and results of EDS analysis of BTTO

Phase	x = 0	x = 0.4	x = 0.6	x = 0.8
a, Å	5.4435 (2)	5.4195 (1)	5.4087 (1)	5.3991 (1)
b, Å	5.4102 (2)	5.3971 (1)	5.3893 (1)	5.3820 (1)
c, Å	32.8640 (9)	32.8406 (6)	32.8250 (5)	32.8097 (6)
g, 10^{-3}	6.14	4.14	3.59	3.17
s.g.	*B2cb*	*B2cb*	*B2cb*	*B2cb*
Cation composition (Bi:Tb:Ti) from EDS analysis	3.98:0:3.02	3.62:0.39:2.99	3.39:0.59:3.02	3.19:0.80:3.01
Bi1/Tb1				
n Bi/Tb	1.00 (2)	0.81/0.19 (2)	0.71/0.29 (2)	0.63/0.37 (2)
x/a	0	0	0	0
y/b	0.9967 (5)	0.9965 (4)	0.9971(4)	0.9973 (5)
z/c	0.0669 (1)	0.0670 (1)	0.0668 (1)	0.0666 (1)
Beq(Å^2)	0.69 (3)	0.65 (5)	0.71 (6)	0.68 (5)
Bi2/Tb2				
n Bi/Tb	0.99 (2)/-	0.99/0.01 (2)	0.98/0.02 (2)	0.97/0.03 (2)
x/a	0.0012 (7)	0.0015 (6)	0.0022 (6)	0.0036 (7)
y/b	0.0125 (8)	0.0129 (6)	0.0133 (4)	0.0136 (7)
z/c	0.2112 (1)	0.2110 (2)	0.2107 (1)	0.2109 (1)
Beq(Å^2)	0.67 (3)	0.57 (3)	0.64 (2)	0.62 (4)
Ti1				
n	1.01 (2)	0.98 (2)	0.99 (2)	0.99 (2)
x/a	0.028 (2)	0.030 (1)	0.0347 (9)	0.0353 (7)
y/b	0	0	0	0
z/c	1/2	1/2	1/2	1/2
Beq(Å^2)	0.46 (2)	0.57 (3)	0.44 (2)	0.62 (4)
Ti2				
n	0.99 (1)	1.01 (2)	1.02 (2)	1.00 (2)
x/a	0.023 (2)	0.029 (2)	0.0035 (12)	0.0038 (12)
y/b	0.0028 (8)	0.0031 (7)	0.0039 (6)	0.0041 (6)
z/c	0.3712 (1)	0.3708 (1)	0.3705 (2)	0.3704 (1)
Beq(Å^2)	0.42 (2)	0.57 (3)	0.40 (2)	0.62 (4)
O1				
n	0.99 (2)	0.99 (2)	0.98 (2)	0.98 (2)
x/a	0.3011 (9)	0.3013 (8)	0.3082 (8)	0.3092 (8)
y/b	0.268 (1)	0.2663 (11)	0.2610 (8)	0.2622 (9)
z/c	0.0040 (3)	0.0080 (4)	0.0121 (3)	0.0110 (2)
Beq(Å^2)	0.92 (5)	0.75 (5)	0.84 (6)	0.78 (5)
O2				
n	1.02 (2)	0.98 (2)	0.99 (2)	0.98 (2)
x/a	0.2835 (12)	0.271 (2)	0.2632 (9)	0.2581 (9)
y/b	0.2591 (9)	0.2521 (8)	0.2513 (8)	0.2498 (7)
z/c	0.2557 (2)	0.2562 (3)	0.2565 (2)	0.2571 (2)
Beq(Å^2)	1.01 (5)	1.07 (4)	1.01 (5)	1.02 (4)
O3				
n	0.98 (2)	0.98 (2)	0.98 (2)	0.99 (2)
x/a	0.065 (2)	0.071 (2)	0.079 (2)	0.0815 (11)
y/b	0.0586 (8)	0.0531 (7)	0.0503 (8)	0.0473 (7)
z/c	0.4412 (3)	0.4409 (2)	0.4406 (3)	0.4407 (2)
Beq(Å^2)	1.26 (6)	1.17 (3)	1.22 (2)	1.21 (4)

Table 1 continued

Phase	x = 0	x = 0.4	x = 0.6	x = 0.8
O4				
n	0.97 (2)	0.98 (2)	0.97 (2)	0.98(2)
x/a	0.0511 (11)	0.055 (1)	0.0673 (11)	0.0661 (11)
y/b	0.946 (1)	0.9522 (8)	0.9672 (9)	0.9612 (8)
z/c	0.3185 (2)	0.3190 (2)	0.3220 (2)	0.3210 (1)
Beq($Å^2$)	1.44 (6)	1.50 (3)	1.39 (2)	1.32 (4)
O5				
n	0.98 (2)	0.97 (2)	0.97 (2)	0.97 (2)
x/a	0.2842 (12)	0.2837 (9)	0.2829 (11)	0.2031 (9)
y/b	0.2580 (8)	0.2568 (7)	0.2560 (7)	0.2552 (8)
z/c	0.1116 (3)	0.1120 (2)	0.1140 (3)	0.1134 (2)
Beq($Å^2$)	1.19 (5)	1.17 (3)	1.14 (2)	1.22 (4)
O6				
n	1.01 (2)	1.01 (2)	1.02 (2)	1.00 (2)
x/a	0.2172 (12)	0.2111 (11)	0.2092 (12)	0.1862 (11)
y/b	0.2117 (8)	0.2142 (7)	0.2161 (7)	0.2272 (8)
z/c	0.8747 (2)	0.8760 (2)	0.8782 (2)	0.8791 (2)
Beq($Å^2$)	0.87 (5)	0.87 (3)	0.94 (2)	0.82 (4)
Rp	5.23	5.51	5.54	5.33
Rwp	6.86	7.06	7.12	7.01
R_B	4.71	5.01	5.04	4.92
χ^2	1.19	1.27	1.31	1.34

Standard deviations of occupation factors are less than 0.02. The orthorhombicity parameter (g) was calculated as $2(a - b)/(a + b)$

the resolution of the instrument. Refinement of the data using the monoclinic model (s.g. $B1a1$) proposed in references [28–31] was not stable owing to strong correlations between the refined parameters. We could not refine our data using any model which had any deviation from orthorhombic symmetry.

The best refinements could be obtained for the model proposed in references [32] and [33] using the orthorhombic space group $B2cb$. Thus, the crystal structure could be described using a polar orthorhombic structure, which is consistent with the fact that the samples showed finite SHG response. The structural parameters for all the compounds are given in Table 1. Corresponding bond distances are shown in Table 2.

Careful analysis of the XRPD patterns revealed that all the samples showed some orthorhombic distortion as seen from the splitting of some reflections, e.g. non coalescence of the (020) and (200) reflections was quite evident even for small doping concentration (x = 0.4).

The remarkable decrease of the orthorhombic distortion (quantified by the orthorhombicity parameter, g, in Table 1) with increase in x can be correlated with the cationic polar displacements and the degree of tilting of the octahedra. The main trends seen in the evolution of the bond distances indicate that the Bi1 cation, located inside the perovskite block, has a coordination number of 12. With an increase in x, the variation of Bi1–O bond lengths gradually decreases and these lengths become more equivalent. A similar situation was observed for Bi2 in the $[Bi_2O_2]$ block in spite of the fact that Bi2 has a different coordination number (9). Coordination around the Ti1 site is relatively insensitive to changes in x. The same tendency was also found for the Ti2 cations. The calculated bond valence sums for the Bi and Ti sublattices gave reasonable values (Table 3), quite close to optimal values. The polyhedral analysis shows drastic off-center displacements for the two Bi atoms, together with distortions of both the Ti octahedral sites. The strong preference for the Bi cations to occupy a highly distorted coordination polyhedral is related to its stereochemically active lone electron pair. In the case of compounds with $x > 0$, when the A-sites are partially occupied by Tb^{3+} instead of Bi^{3+}, the observed orthorhombic distortion is significantly less and these polyhedra are more regular.

Our investigations suggest that incorporation of Tb occurs at both the Bi^{3+} sites, but a substitution at the Bi1 site in the perovskite layer is more favorable.

Table 2 Selected bond distances and angles from XRPD powder refinements of BTTO at room temperature

Cation	x = 0	x = 0.4	x = 0.6	x = 0.8
Bi1/Tb1				
O5	2.301	2.308	2.304	2.288
O3	2.402	2.355	2.353	2.334
O3	2.411	2.438	2.422	2.369
O6	2.519	2.470	2.454	2.469
O5	2.559	2.554	2.459	2.472
O1	2.659	2.560	2.584	2.562
O1	2.853	2.878	2.836	2.852
O6	2.904	2.922	2.836	2.858
O1	3.020	2.961	3.020	3.002
O3	3.072	3.039	3.067	3.029
O3	3.102	3.117	3.151	3.155
O1	3.189	3.279	3.378	3.352
Bi2/Tb2				
O2	2.179	2.183	2.205	2.206
O2	2.252	2.297	2.269	2.237
O2	2.329	2.318	2.355	2.282
O2	2.506	2.450	2.427	2.408
O4	2.555	2.583	2.592	2.587
O4	2.647	2.620	2.644	2.647
O4	3.156	3.163	3.204	3.171
O4	3.228	3.197	3.242	3.215
O6	3.289	3.309	3.354	3.327
Ti1				
O1X2	1.909	1.916	1.908	1.896
O3X2	1.950	1.955	1.982	1.978
O1X2	1.969	1.974	1.998	1.994
Ti2				
O4	1.766	1.729	1.692	1.684
O6	1.875	1.826	1.796	1.768
O5	2.000	1.997	1.959	1.960
O6	2.016	2.014	2.019	2.034
O5	2.024	2.072	2.115	2.139
O3	2.331	2.328	2.326	2.329

Standard deviation is less than 0.009 for cations and less than 0.03 for anions

3.2 IR spectroscopy

The IR spectra of all the samples are characterized by the same set of absorption bands (Fig. 3). This shows that all the BTTO solid solutions are isostructural to BTO, in agreement with the conclusions drawn from the XRPD results. The valence vibrations of the Ti–O bonds in the TiO_6 octahedra of the perovskite layers appear in the form of two wide absorption bands in the IR spectra in the range of ~870–800 and ~740–530 cm^{-1}. The maxima of these bands shift towards higher frequency with an increase in x. The observed shift indicates a decrease in the Ti–O bond lengths and an increase in their energy. Furthermore, the decrease in the intensity of the absorption band at ~870–800 cm^{-1} indicates an increase in the concentration of Tb^{3+} cations. The decrease in the Ti–O bond lengths with an increase in x is connected to changes in the electronic configuration and, hence, a smaller ionic radius of the Tb^{3+} cations compared to Bi^{3+} ions. Therefore, the introduction of Tb^{3+} into the perovskite layers leads to a displacement of the TiO_6 octahedra along the *a* axis, and to a change of the Ti–O valence bond angle [34]. These results are in agreement with the conclusion drawn from the XRPD data i.e., the Tb^{3+} cations are preferentially substituted at the Bi^{3+} sites of the perovskite layers of the BTTO crystal structure (Table 1). The decrease in the intensity of the absorption band at ~870–800 cm^{-1} indicates that the BTTO compositions approach the concentration phase transition boundary from orthorhombic to tetragonal symmetry with increasing x that is also evident in the decrease of their orthorhombicity parameter.

3.3 Second harmonic generation (SHG) response

The second harmonic signal as a function of Tb concentration (x) is shown in Fig. 4. We do not show data on the undoped BTO in Fig. 4 since the microstructure and crystallite size of the undoped sample differ from that of the doped samples. However, previous reports suggest that the intensity of the signal at room temperature for undoped BTO is greater than 200 [35]. In comparison, the doped samples exhibit lower values of the second harmonic signal (Fig. 4). This is expected because non-centrosymmetry is largest in undoped BTO. Introduction of Tb in the structure leads to a monotonous decrease in the non-centrosymmetry, as seen in Fig. 4. This tendency is in line with our conclusions from the analysis of the XRPD data, which also indicate a decrease in the orthorhombic distortion of the crystal structure with an increase in the Tb concentration. The formation of a more regular crystal structure with low cation displacement inside the oxygen polyhedra leads to a decrease in the electrical polarization.

3.4 Thermal analysis

The electric ordering-disordering in the crystal structure of BTO is accompanied by a structural phase transition from orthorhombic to tetragonal symmetry. Reversible thermal effects related to this transition in BTTO ($0 \leq x \leq 0.4$) are visible in the DTA curves (Fig. 5). The magnitude of the endothermic/exothermic peaks decreases with an increase in x and they become broader. The concentration of the Tb^{3+} ions i.e., x has a strong influence on the

Table 3 Polyhedral analysis of BTTO at 295 K

Cation	x	δ (Å)	ξ (Å)	V (Å^3)	Δ	Valence
Bi1/Tb1 (c.n. = 12)	0	0.042	2.749 ± 0.311	48.2 (1)	0.072	2.88
	0.4	0.057	2.740 ± 0.329	47.8 (1)	0.068	2.86
	0.6	0.089	2.737 ± 0.355	47.6 (1)	0.069	2.97
	0.8	0.091	2.729 ± 0.358	47.3 (1)	0.067	3.06
Bi2/Tb2 (c.n. = 9)	0	0.419	2.682 ± 0.434	36.6 (1)	0.098	2.93
	0.4	0.416	2.680 ± 0.430	36.8 (1)	0.096	2.91
	0.6	0.387	2.691 ± 0.449	37.2 (1)	0.091	2.85
	0.8	0.379	2.687 ± 0.438	37.3 (1)	0.088	2.91
Ti1 (c.n. = 6)	0	0.128	1.943 ± 0.027	9.6 (1)	0.011	4.13
	0.4	0.121	1.941 ± 0.027	9.7 (1)	0.010	4.16
	0.6	0.098	1.963 ± 0.043	9.8 (1)	0.016	4.04
	0.8	0.096	1.956 ± 0.047	9.8 (1)	0.015	4.11
Ti2 (c.n. = 6)	0	0.037	1.984 ± 0.019	10.3 (1)	0.013	3.94
	0.4	0.051	1.995 ± 0.208	10.1 (1)	0.016	4.13
	0.6	0.057	1.973 ± 0.246	9.7 (1)	0.020	4.18
	0.8	0.061	1.979 ± 0.248	9.8 (1)	0.021	4.16

δ—cation shift from centroid, ξ—average bond distance, V—polyhedral volume, Δ—polyhedral volume distortion

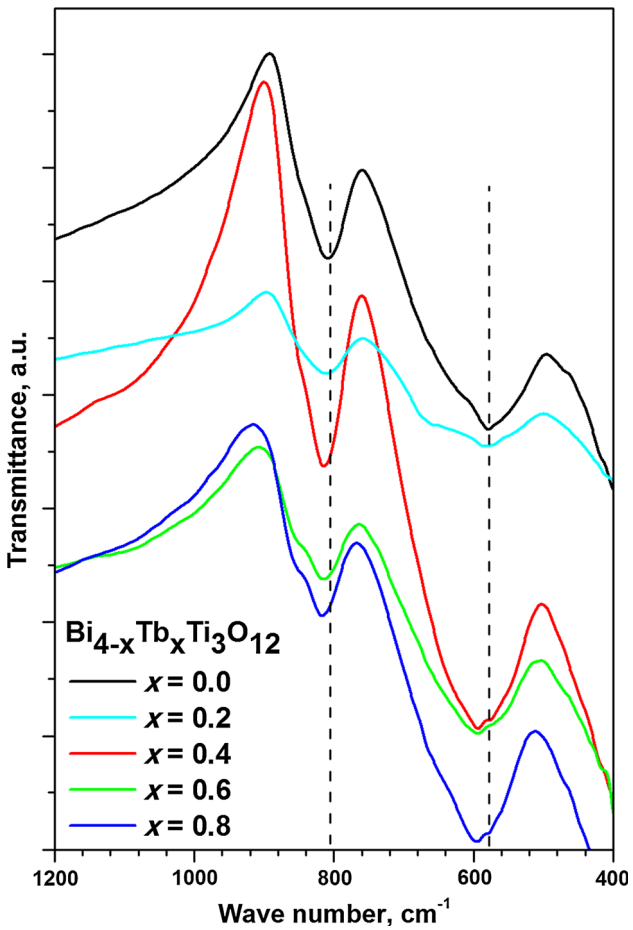

Fig. 3 IR spectra of BTTO

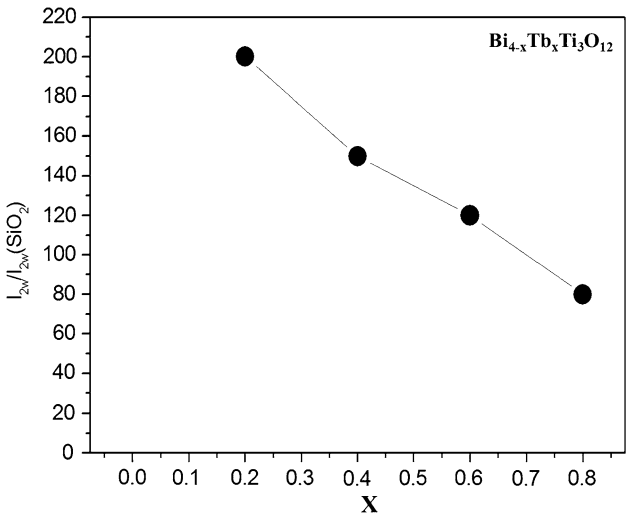

Fig. 4 Second harmonic signal as a function of Tb concentration (x) in BTTO

orthorhombicity of the crystal structure. The decrease in orthorhombicity with increase in x, revealed by the XRPD studies, indicates an approach towards the concentration boundary of orthorhombic phase formation. Therefore, the temperature of the structural transition decreases with an increase in the Tb^{3+} content. This tendency in BTTO samples is consistent with the XRPD results that revealed that the *a* and *b* unit cell parameters become closer and the orthorhombicity parameter decreases as x increases (Table 1). In the BTTO samples with $x \geq 0.6$, the effects related to the phase transition could not be observed in the DTA curves. This indicates that changes in the crystal

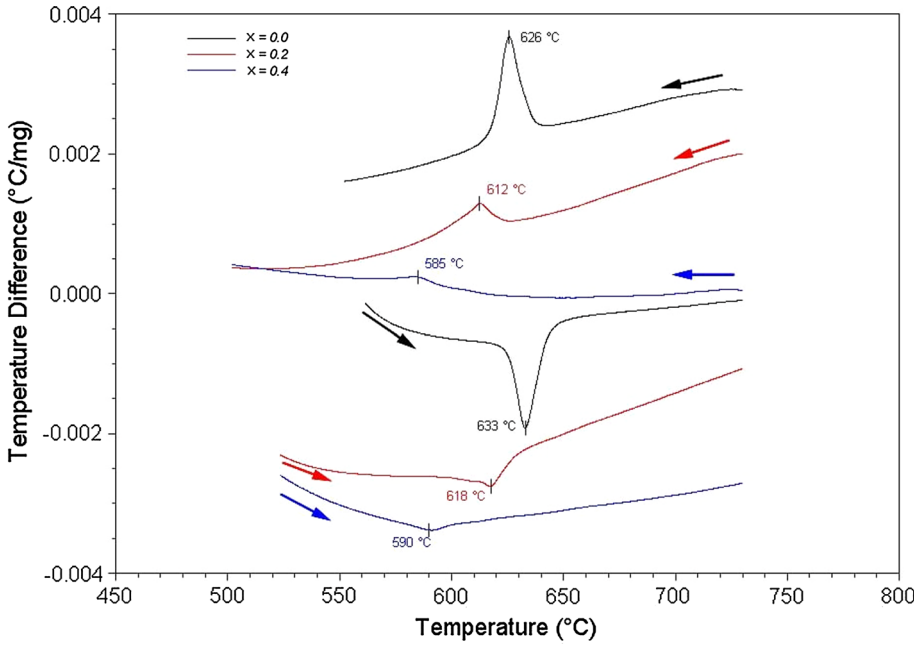

Fig. 5 DTA curves of BTTO

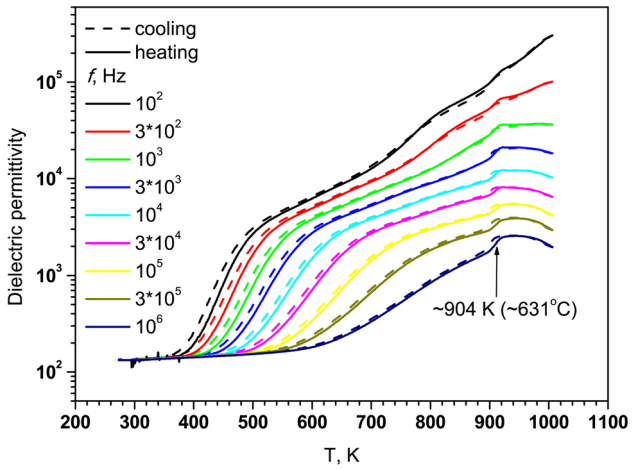

Fig. 6 Real part of dielectric permittivity (ε') versus T at different frequencies for BTO

structure of BTTO with x = 0.6 and 0.8 are second order in nature.

3.5 Dielectric spectroscopy

The temperature and frequency dependence of the real part of dielectric permittivity (ε') of the BTTO ceramics are shown in Fig. 6 (x = 0) and Fig. 7 (x > 0). Two types of anomalies can be seen, the first being frequency dependent in the range 400–700 K, and related to the relaxation processes in the ceramics [36, 37]. The second type of anomaly, connected to the ferroelectric phase transition in the samples, can be seen for $0 \leq x \leq 0.4$. These anomalies (marked by black arrows in Figs. 6 and 7) are frequency independent and have low hysteresis. The temperature of the ferroelectric phase transition shows a decreasing tendency with an increase in the value of x. The ferroelectric phase transition temperatures as estimated from the dielectric spectroscopy results show a good agreement with those estimated from the DTA curves. For x = 0.6, the second anomaly becomes frequency dependent, and relaxation processes dominate the dielectric response above this concentration. The decrease in the phase transition temperature of the BTTO series with an increase in x can be related to the decrease of volume and orthorhombic distortion of the unit cell with an increase in x as revealed by the XRPD studies.

3.6 Magnetic measurements

The M versus T curves of the BTTO series recorded in the zero field cooled mode under a low field (H = 0.005 T) and a high field (H = 0.5 T) are shown in Fig. 8a, b respectively. The samples are paramagnetic and do not show any magnetic transition in the measured temperature range of 5–320 K.

In order to investigate the paramagnetic behaviour of BTTO further, we performed Curie–Weiss fits to the susceptibility data using the modified Curie–Weiss law, $\chi = \chi_0 + \frac{C}{T-\theta_{CW}}$. As representative examples, we show the fits for the two end members (x = 0 and 0.8) in Fig. 9.

The values of the effective magnetic moment (μ_{eff}) and the Curie–Weiss constants (θ_{CW}) obtained from the fits for the entire BTTO series are summarized in Table 4. There is a good agreement between the calculated spin only

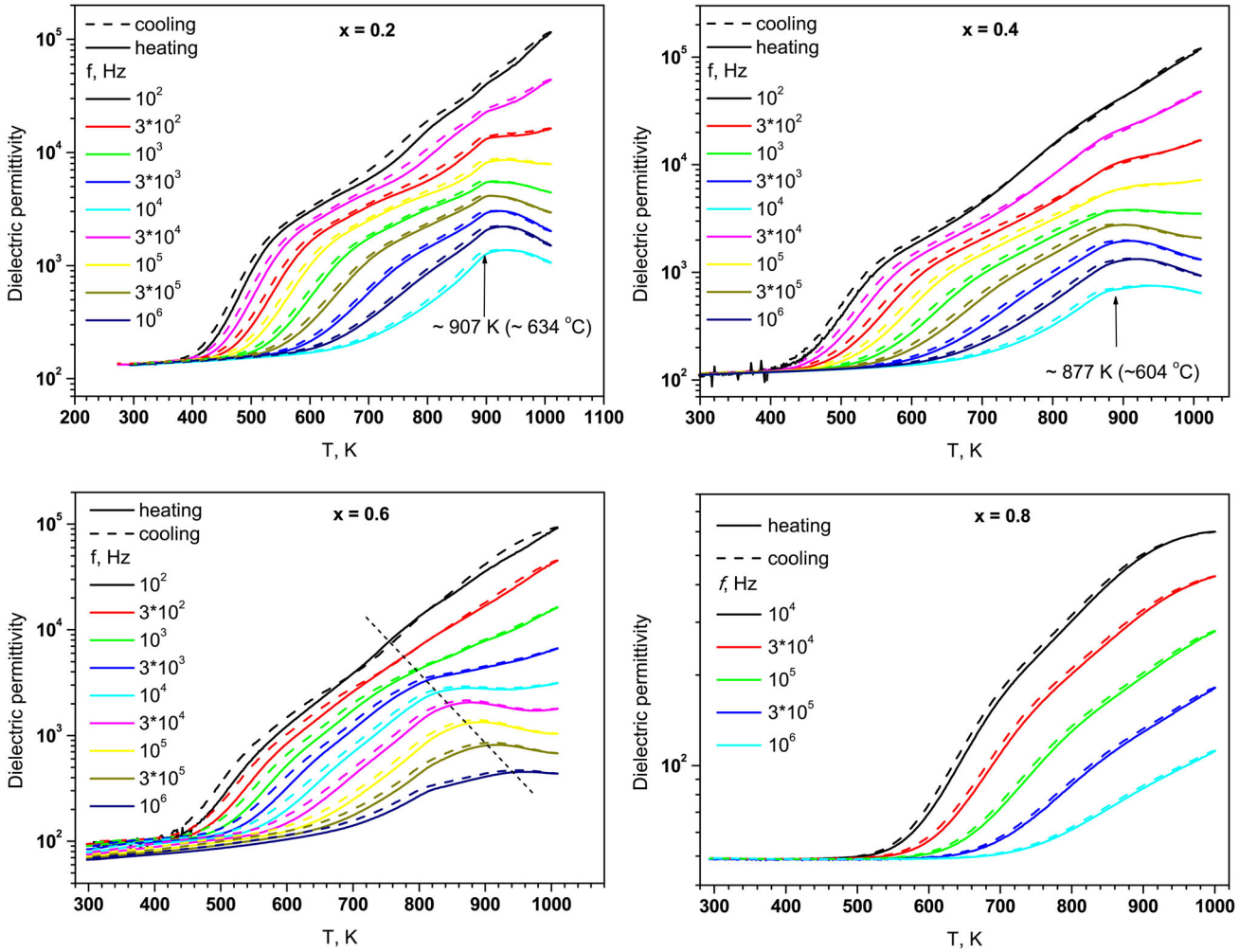

Fig. 7 Real part of dielectric permittivity (ε') versus T at different frequencies for BTTO

moment per formula unit and the effective magnetic moment extracted from our fits to the experimental data. Furthermore, all the samples have a very small negative value of the Curie–Weiss constant close to zero. Thus, an incorporation of Tb^{3+} at the A-site does not give rise to any appreciable magnetic correlation in the samples.

4 Conclusion

We have synthesized the Aurivillius phase $Bi_{4-x}Tb_xTi_3O_{12}$ with x ranging from 0 to 0.8, and studied their detailed crystal structure, dielectric, and magnetic properties. All the samples showed finite SHG response indicating a non-cen-

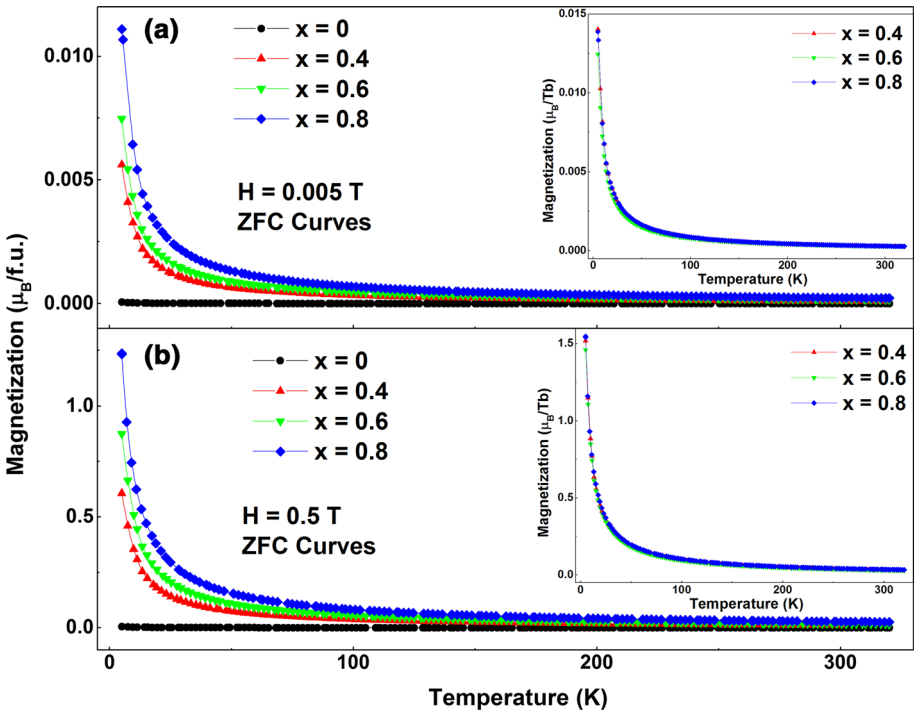

Fig. 8 M versus T curves of BTTO recorded under a magnetic field of **a** H = 0.005 T and **b** H = 0.5 T. The *insets* show the same curves for the doped samples with the magnetization plotted in units of μ_B/Tb

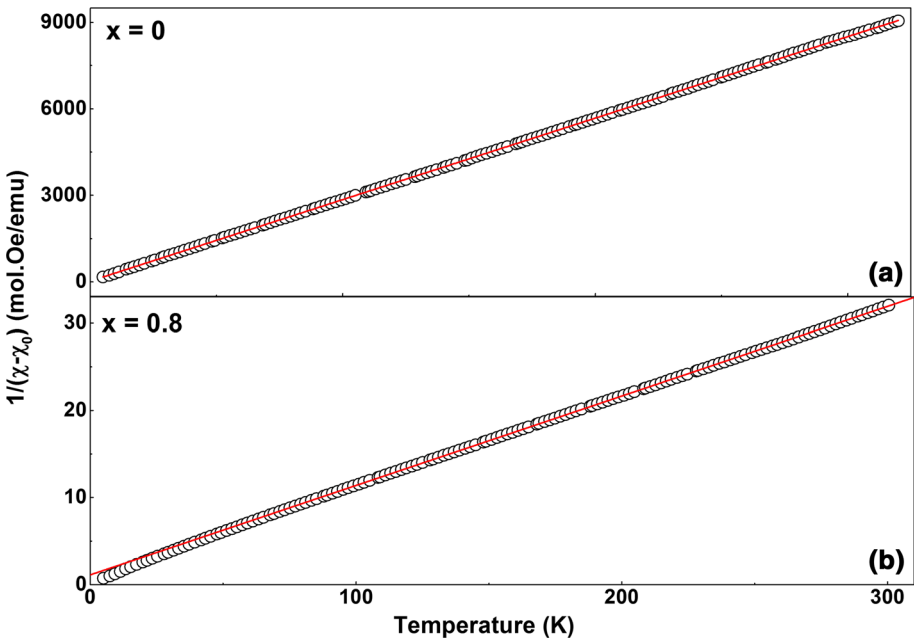

Fig. 9 Inverse magnetic susceptibility versus temperature for **a** BTO and **b** $Bi_{3.2}Tb_{0.8}Ti_3O_{12}$. The *straight lines* are the fits to the experimental data (see text for details)

trosymmetric structure. The IR spectroscopy results revealed that all the solid solutions of BTTO are isostructural to BTO, but with a decrease in the Ti–O bond lengths as x increased. A detailed analysis of the structural data using a polar orthorhombic space group revealed a decrease in the orthorhombicity with an increase in x. The ferroelectric phase transition temperatures were estimated using multiple measurement techniques such as thermal analysis (DTA curves) and dielectric spectroscopy. The results obtained from the two techniques were found to be in good agreement with each other. A decrease in the Curie temperature value with an increase in x, and a cross-over to a relaxor-type behavior for higher values of x was observed. The samples are paramagnetic in the temperature range 5–320 K.

Table 4 Effective magnetic moments (μ_{eff}) and Curie–Weiss constants (θ_{CW}) of BTTO obtained from Curie–Weiss fits to the high temperature susceptibility data

x	μ_{eff}/f.u. (μ_B)	θ_{CW} (K)	μ_{calc} (μ_B)
0	0.53	−1	0
0.4	5.63	−2	6.15
0.6	7.35	−4	7.53
0.8	8.09	−3	8.69

Acknowledgements Financial support from the Swedish Research Council (VR), the Swedish Foundation for International Cooperation in Research and Higher Education (STINT), and the Russian Foundation for Basic Research (Project No. 15-03-01676) is gratefully acknowledged. We thank S. Yu. Stefanovich for his technical assistance with the SHG experiments.

Open Access This article is distributed under the terms of the Creative Commons Attribution 4.0 International License (http://creativecommons.org/licenses/by/4.0/), which permits unrestricted use, distribution, and reproduction in any medium, provided you give appropriate credit to the original author(s) and the source, provide a link to the Creative Commons license, and indicate if changes were made.

References

1. S.-W. Cheong, M. Mostovoy, Nat. Mater. **6**, 13 (2007)
2. W. Eerenstein, N.D. Mathur, J.F. Scott, Nature **442**, 759 (2006)
3. J.F. Scott, Nat. Mater. **6**, 256 (2007)
4. M. Bibes, A. Barthélémy, Nat. Mater. **7**, 425 (2008)
5. A. Roy, R. Gupta, A. Garg, Adv. Condens. Matter Phys. **2012**, 926290 (2012)
6. Y. Wang, J. Hu, Y. Lin, C.-W. Nan, NPG Asia Mater. **2**, 61 (2010)
7. J. Ma, J. Hu, Z. Li, C.-W. Nan, Adv. Mater. **23**, 1062 (2011)
8. A. Peláiz-Barranco, Y. González-Abreu, J. Adv. Dielectr. **3**, 1330003 (2013)
9. E.C. Subbarrao, J. Phys. Chem. Solids **23**, 665 (1962)
10. H. Nagata, T. Tokutsu, D. Nakai, Y. Hiruma, T. Takenaka, Ferroelectrics **368**, 202 (2008)
11. M. Villegas, A.C. Caballero, C. Moure, P. Durán, J.F. Fernández, J. Am. Ceram. Soc. **82**, 2411 (1999)
12. G.A. Smolenskii, V.A. Isupov, A.I. Agranovskaya, Sov. Phys. Solid State **1**, 149 (1959)
13. E.C. Subbarrao, Phys. Rev. **122**, 804 (1961)
14. B.H. Park, B.S. Kang, S.D. Bu, T.W. Noh, J. Lee, W. Jo, Nature **401**, 682 (1999)
15. N.A. Benedek, J.M. Rondinelli, H. Djani, P. Ghosez, P. Lightfoot, Dalton Trans. **44**, 10543 (2015)
16. F.-Q. Zhang, Y.-X. Li, J. Inorg. Mater. **29**, 449 (2014)
17. X.Q. Chen, F.J. Yang, W.Q. Cao, H. Wang, C.P. Yang, D.Y. Wang, K. Chen, Solid State Commun. **150**, 1221 (2010)
18. V.A. Khomchenko, G.N. Kakazeim, Y.G. Pogorelov, Y.G. Pogorelov, J.P. Araujo, M.V. Bushinsky, D.A. Kiselev, A.L. Kholkin, J.A. Paixão, Mater. Lett. **64**, 1066 (2010)
19. R. Muralidharan, T.H. Jang, C.H. Yang, Y.H. Jeong, S.H. Kang, I.W. Kim, T.Y. Koo, J. Phys: Conf. Ser. **200**, 012135 (2010)
20. T. Shigyo, H. Kiyono, J. Nakano, H. Itoh, J. Takahashi, Jpn. J. Appl. Phys. **47**, 7617 (2008)
21. P. Zhou, Z. Mei, C. Yang, Y. Qi, K. Liang, Z. Ma, T. Zhang, J. Mater. Sci.: Mater. Electron. **27**, 7755 (2016)
22. H. Qi, Y. Qi, M. Xiao, J. Mater. Sci.: Mater. Electron. **25**, 1325 (2014)
23. X.A. Mei, M. Chen, C.Q. Huang, R.F. Liu, Key Eng. Mater. **633**, 265 (2015)
24. K. Momma, F. Izumi, J. Appl. Cryst. **44**, 1272 (2011)
25. E.A. Fortalnova, E.D. Politova, S.A. Ivanov, M.G. Safronenko, Russ. J. Inorg. Chem. **62**, 1 (2017)
26. J.R. Carvajal, Phys. B **192**, 55 (1999)
27. V.B. Kalinin, SYu. Stefanovich, Cation mobility in orthophosphates: the results of science and technology. Ser. Solid State Chem. **8**, 1–131 (1992)
28. R.D. Shannon, Acta Cryst. A **32**, 751 (1976)
29. A.D. Rae, J.G. Thompson, R.L. Withers, A.C. Willis, Acta Cryst. **B46**, 474 (1990)
30. M.K. Jeon, S.I. Woo, Y.-I. Kim, S.-H. Nahm, J. Korean Phys. Soc. **45**, 1240 (2004)
31. J.M. Perez-Mato, P. Blaha, K. Schwarz, M. Aroyo, D. Orobengoa, I. Extebarria, A. García, Phys. Rev. B **77**, 184104 (2008)
32. J.F. Dorrian, R.E. Newnham, D.K. Smith, M.I. Kay, Ferroelectrics **3**, 17 (1972)
33. C.H. Hervoches, P. Lightfoot, Chem. Mater. **11**, 3359 (1999)
34. Y.-M. Kan, G.-J. Zhang, P.-L. Wang, Y.-B. Cheng, J. Eur. Ceram. Soc. **28**, 1641 (2008)
35. A.M. Kusainova, SYu. Stefanovich, J.T.S. Irvine, P. Lightfoot, J. Mater. Chem. **12**, 3413 (2002)
36. A. Subohi, L. Shastri, G.S. Kumar, M.M. Malik, R. Kurchania, Mater. Res. Bull. **49**, 651 (2014)
37. S. Rachna, S.M. Gupta, S. Bhattacharyya, Pramana J. Phys. **71**, 599 (2008)